Physica B 404 (2009) 4007–4014

Contents lists available at ScienceDirect

Physica B

journal homepage: www.elsevier.com/locate/physb

Nanoscale ab-initio calculations of optical and electronic properties of $LaCrO_3$ in cubic and rhombohedral phases

N. Soltani, S.M. Hosseini *, A. Kompany

Department of Physics (Materials and Electroceramics Laboratory), Ferdowsi University of Mashhad, Iran

ARTICLE INFO

Article history:
Received 15 November 2008
Received in revised form
24 February 2009
Accepted 13 July 2009

PACS:
71.15.Mb
71.22.+i
74.25.Jb

Keywords:
$LaCrO_3$
Ab initio calculations
Density functional theory
Electronic structure
Optical properties

ABSTRACT

We report nanoscale ab-initio calculations of the linear optical and electronic properties of $LaCrO_3$ in nonmagnetic cubic and rhombohedral phases using the full potential linear augmented plane wave (FP-LAPW) method. In this work the generalized gradient approximation is used for exchange-correlation potential. The dielectric tensor is derived within random-phase approximation. We present results for the band structure, density of states, imaginary and real parts of dielectric tensor, electron energy loss spectroscopy, sum rules, reflectivity, refractive index and extinction coefficient. The regions of transparent, absorption and reflection are discussed. We are not aware of any published experimental or theoretical data for these phases, so our calculations can be used to cover this lack of data for these phases.

1. Introduction

The ABO_3 type perovskite crystals have been extensively studied because of their technical importance and the fundamental interest in the physics of their phase transitions. The perfect perovskite structure is very simple and has full cubic symmetry in which the body center position is occupied by B atoms, the edges by A atoms and the face centers by oxygen atoms in Pm3m space group [1]. $LaCrO_3$ structure is considered to be a pseudo-perovskite, or distorted perovskite, and has been studied widely, focusing on various industrial uses above room temperature, for example, may act as a spacer as well as an interconnects in solids oxide fuel cells and high density magneto optical (MO) disks [2]. At some temperatures between 200 and 260 °C it undergoes a crystallographic transformation from orthorhombic to rhombohedral structure, in which volume changes.

At room temperature the phase transitions occurs at around $T = 18$ °C (Neel temperature) [3]. This is due to magnetic order disorder transitions. The structural phase transition to cubic symmetry was suggested to occur above 1600 °C, but it is not fully understood because of its experimental difficulty [4].

However, the theoretical aspects of optical and electronic properties of $LaCrO_3$ have been relatively rarely studied, and a few experimental articles on orthorhombic phase of this material have been published. Armia et al. [5] have reported a systematic experimental study of optical gap around 4 eV in $LaCrO_3$. Ravindran et al. [2] have calculated the electronic structure and linear optical properties for the series $LaXO_3$ (X = Sc–Cu). They used local spin–density approximation (LSDA+U) in order to provide the right insulating properties of perovskites. The band gap and optical gap have obtained were about 1.45 and 3.5 eV, respectively. Ong et al. [6] have calculated the electronic structure and optical properties of $LaCrO_3$ in orthorhombic phase.

In this paper the scheme of optical and electronic properties of nonmagnetic cubic and rhombohedral phases in nanoscale has been studied using the full potential linearized augmented plane wave method (FP–LAPW) by Wien2k codes [8]. However, to our knowledge no previous theoretical and experimental results have been seen to compare with the results of this paper.

2. Computational details

Our calculations are based on the density functional theory (DFT). The Perdew–Burke–Ernzerhof generalized gradient approximation (GGA) was used for the exchange correlation correction

* Corresponding author. Tel.: +98 511 8435723; fax: +98 511 8796416.
E-mail address: sma_hosseini@yahoo.com (S.M. Hosseini).

0921-4526/$ - see front matter © 2009 Elsevier B.V. All rights reserved.
doi:10.1016/j.physb.2009.07.151

[9,10]. The density of states is deduced from a self-consistent calculation, using the full potential linearized augmented plane wave (FP-LAPW) method and the dielectric function is obtained by random phase approximation (RPA), as embodied in the Wien2k code. The convergence of the basis set is controlled by a cut off parameter $R_m \times k_{\max} = 7$ and 6 for cubic and rhombohedral phases, respectively. The values of other parameters are $G_{\max} = 14$ (magnitude of largest vector in charge density Fourier expansion or the plane wave cutoff), $R_{MT}(\mathrm{La}) = 2.6$ au, $R_{MT}(\mathrm{Cr}) = 1.8$ au and $R_{MT}(\mathrm{O}) = 1.6$ au (muffin-tin radius). The iteration halted when the difference charge was less than 0.0001e between steps as convergence criterion. The cut off energy, which defines the separation of valence and core states, was chosen as -6 Ry. In these calculations, we neglected the effect of spin orbit coupling.

The imaginary part of the dielectric tensor can be computed from the knowledge of the electronic band structure of a solid. In the limit of linear optics, in the case of nonspinpolarized, and within the frame of random-phase approximation we can use the following well-known relations [12] for a vertical transition from a filled initial state of energy $E_{n,k}$ to an empty final state of energy $E_{n',k}$ with wave vector k.

$$\mathrm{Im}\,\varepsilon_{ij}(\omega) = \frac{\hbar^2 e^2}{\pi m^2 \omega^2} \sum_{n,n'} \int_k p_{i;n'}, n, k p_{j;n'}, n, k (f_0(E_{n,k}) - f_0(E_{n'}, k)) \delta(E_{n'}, k - E_{n,k} - \hbar\omega) \quad (1)$$

where ω is the frequency, e the electron charge, m the free electron mass, $p_{i;n,n',k}$ and $p_{j;n,n',k}$ the momentum matrix elements between states of bands n and n' with crystal momentum k in directions i and j, respectively [13]. The corresponding real parts are obtained by Kramers–Kronig transformation as follows:

$$\mathrm{Re}\,\varepsilon_{ij}(\omega) = \delta_{ij} + \frac{2}{\pi} P \int \frac{\omega' \,\mathrm{Im}\,\varepsilon_{ij}(\omega')}{\omega'^2 - \omega^2} d\omega' \quad (2)$$

where P is the principal part of the Cauchy integral.

In order to get the isotropic dielectric function, the components of the electric matrix trace are averaged, i.e. $\varepsilon_{iso} = 1/3(\varepsilon_{xx} + \varepsilon_{yy} + \varepsilon_{zz})$ [14].

The optical conductivity is given by

$$\mathrm{Re}\,\sigma_{ij}(\omega) = \frac{\omega}{4\pi} \mathrm{Im}\,\varepsilon_{ij}(\omega) \quad (3)$$

Moreover, the real and imaginary parts of complex refractive index $N(\omega)$ and extinction coefficient is given by

$$n_{ij}(\omega) = \sqrt{\frac{|\varepsilon_{ij}(\omega)| + \mathrm{Re}\,\varepsilon_{ij}(\omega)}{2}} \quad (4)$$

$$k_{ij}(\omega) = \sqrt{\frac{|\varepsilon_{ij}(\omega)| - \mathrm{Re}\,\varepsilon_{ij}(\omega)}{2}} \quad (5)$$

Besides, in the low-region of the electron energy loss spectrum (EELS) interband transitions and plasmon losses are observed and can provide information about compositions, electronic structure and optical properties. The EELS is related to dielectric tensor by

$$L_{ij}(\omega) = -\mathrm{Im}\left(\frac{1}{\varepsilon(\omega)}\right)_{ij} = \frac{\mathrm{Im}\,\varepsilon_{ij}}{(\mathrm{Re}\,\varepsilon_{ij})^2 - (\mathrm{Im}\,\varepsilon_{ij})^2} \quad (6)$$

The reflectivity at normal indices is

$$R_{ij}(\omega) = \frac{(n_{ij} - 1)^2 + k_{ij}^2}{(n_{ij} + 1)^2 + k_{ij}^2} \quad (7)$$

The dielectric tensor must obey certain sum rules that serve to check accuracy of the calculation and also, provide information about the absorption process that can be checked experimentally. The sum rule relation is given by

$$\int_0^{\omega'} \mathrm{Im}\,\varepsilon_{ij}(\omega)\, d\omega = N_{eff}(\omega') \quad (8)$$

This $N_{eff}(\omega)$ is the number of electronic contributing to the absorption process as a function of energy [12].

At low frequency the static refractive index $n_{ij}(0)$ can be calculated using the following expression for nonmagnetic materials:

$$n_{ij}^2(0) = \mathrm{Re}\,\varepsilon_{ij}(\infty) \quad (9)$$

For the dielectric tensor calculations, the Brillouin zone (BZ) integrals were made with 56 and 182 independent k-points for cubic and rhombohedral phases, respectively.

Table 1
Calculated lattice parameters of $LaCrO_3$ for cubic and rhombohedral phases.

Structure	Experimental (Å)	Space group	Lattice parameters (Å)
Cubic	$a = 3.92$ [7]	Pm3m	$a = 3.85$
Rhombohedral (hcp axes)	$a = b = 5.53$, $c = 13.35$ [4]	$R\bar{3}c$	$a = b = 5.51$, $c = 13.39$

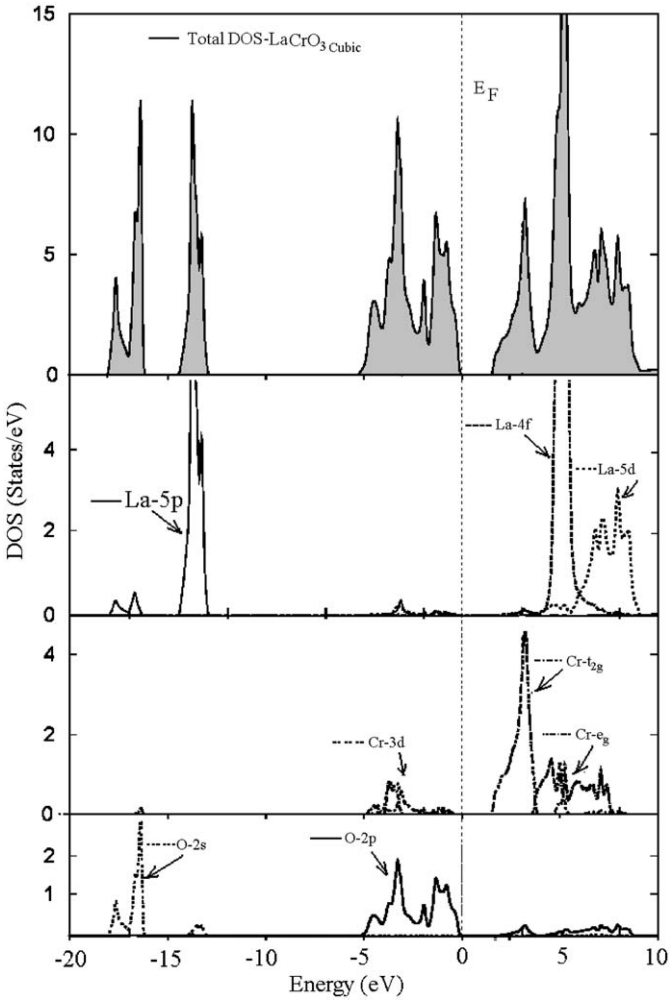

Fig. 1. Total and partial DOS of $LaCrO_3$ in cubic phase.

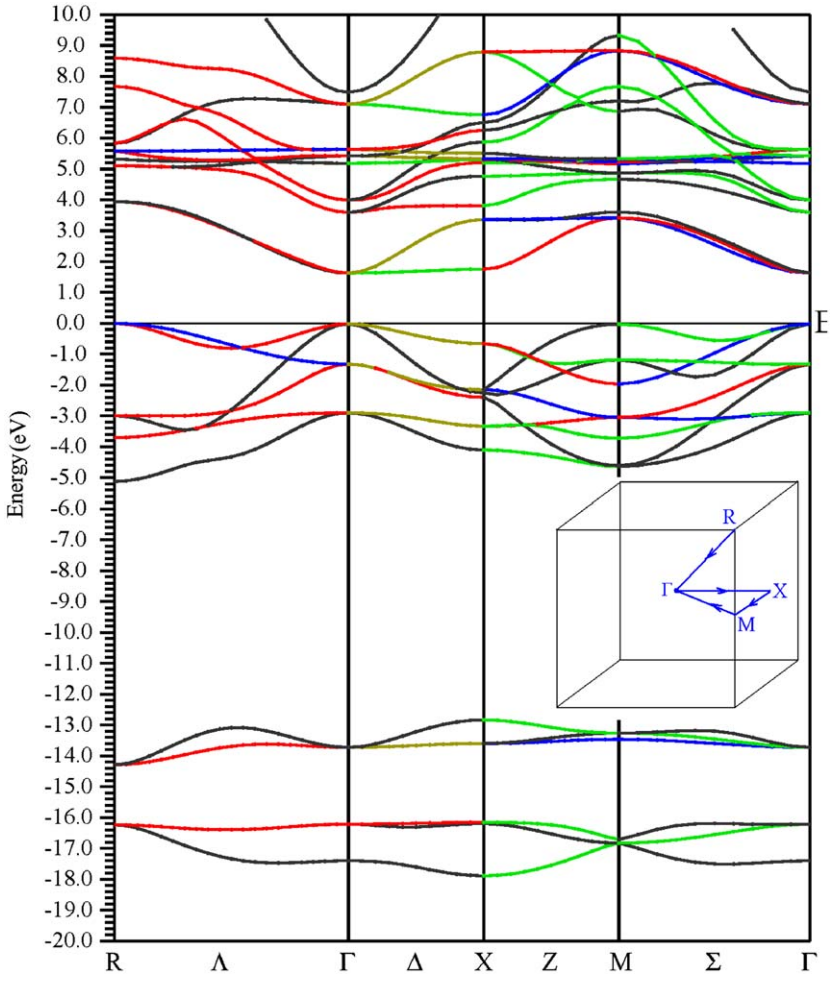

Fig. 2. Band structure of $LaCrO_3$ in cubic phase and the primitive Brillouin zone.

3. Results and discussions

3.1. Structure

$LaCrO_3$ undergoes a crystallographic transformation from orthorhombic to rhombohedral structure at some temperatures between 200 and 260 °C. The discrete volume compression was observed at the phase transition from orthorhombic to rhombohedral phase. The structural phase transition to cubic symmetry was suggested to occur above 1600 °C, but it is not fully understood because of its experimental difficulty [4]. $LaCrO_3$ in orthorhombic phase is observed in Pnma space group (no. 62) [1], in rhombohedral phase in $R\bar{3}c$ (no. 167) [4] and in cubic phase with Pm3m space group (no. 221) [7].

To calculate the electronic properties of rhombohedral structure using Wien2k codes, the hexagonal lattice constants (a_h, c_h) must be specified as input parameters. Conversion from rhombohedral lattice constant (a_r) to hexagonal has been done using the following relations:

$$a_h = 2\cos\left(\frac{\pi - \alpha_r}{2}\right)a_r$$

$$c_h = 3\sqrt{a_r^2 - (1/3)a_h^2} \tag{10}$$

The calculations were first carried out by applying the experimentally observed structural parameters [4,7]. Then by minimizing the total energy of the crystal to the volume, the theoretical lattice constants were obtained. For rhombohedral phase, by fixing the experimental volume of primitive cell, energy has been optimized according to the ratio of c/a. The calculated results in this work and the values obtained by the other methods are summarized in Table 1.

The final calculation was performed with the theoretical lattice constant and relaxed structure.

3.2. Electronic properties

The total and partial density of states (DOS) of $LaCrO_3$ in the cubic phase is depicted in Fig. 1 where the contribution of Cr-t_{2g} and e_g bands has been shown. The band structure of $LaCrO_3$ in the cubic phase along some high symmetry directions of Brillouin zone is depicted in Fig. 2.

For rhombohedral phase, the band structure is displayed in Fig. 3. For cubic and rhombohedral phases, the upper valence band index is 20 and 40, respectively.

For cubic phase, an indirect band gap of 1.63 eV (without correction factor) is seen in the direction R–Γ, between the top of valence band at point R and the bottom of conduction band at point Γ whereas a direct gap of 1.56 eV is seen in the direction of Γ–Γ. In cubic structure, it is seen that the top of the valence band has a parabolic shape in the directions of R–Γ, R–X, M–Γ which shows that the effective mass is the same in these directions, so

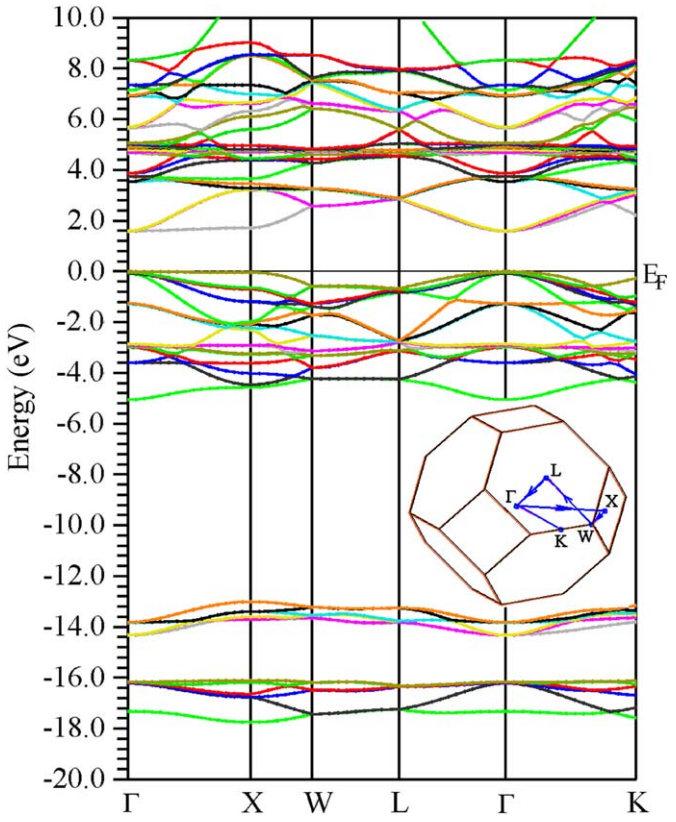

Fig. 3. Band structure of $LaCrO_3$ in rhombohedral phase and the primitive Brillouin zone. For primitive Brillouin zone, we used xcrysden (x-window CRYstalline Structures and DENsities) [11].

we expect an isotropy in electronic properties of this material in reported directions.

For rhombohedral phase, the contribution of Cr-3d levels in band structure is also depicted in Fig. 4. In the hexagonal closed pack phase, hcp, which can be converted to rhombohedral, Cr-3d bands are divided into three levels of $d_{x^2-y^2}+d_{xy}$, d_{z^2} and $d_{xz}+d_{yz}$ which show a decrease in the degeneracy of t_{2g} and e_g bands. This shows Jahn Teller effect which has occurred due to the protraction of CrO_6 octahedral. The gradient of valence band around Γ in the Γ–K and Γ–L directions is slightly parabolic shape, whereas in Γ–X direction it is a plateau. So, we expect to have anisotropy in electronic property just in two directions. In both structures the hybridation of O-2p and Cr-3d causes the electronic of oxygen to participate in conductance. In Figs. 3(a), (b) and (c), the contribution of Cr in band structure is shown as empty circles on the band structure for $Cr-d_{x^2-y^2}+d_{xy}$, $Cr-d_{z^2}$ and $Cr-d_{xz}+d_{yz}$, respectively.

3.3. Optical properties

3.3.1. Dielectric function

Fig. 5 shows the variation of the imaginary part of the dielectric function within GGA approximation for cubic and rhombohedral phases, for radiation up to 30 eV. For cubic and rhombohedral structure, we expect the same response for the diagonal elements of dielectric tensor in directions of x, y and z. For both structural phases, there are two main peaks around 8 and 21 eV, the former is related to transitions from O-2p to Cr-3d and the latter is probably related to transitions from La-5p to Cr-3d and then to La-4f.

According to the quasi-pole approximation used in the base of calculations, the selection rules of $\Delta l=\pm 1$ should be considered whereas $\Delta l=\pm 2$ (related to quadropole term) should be neglected. Thus, transitions from La-5p to La-4f occur via the middle transition of La-5p to Cr-3d.

The real part of the dielectric tensor is related to dispersion, which is displayed in Fig. 6 for cubic and rhombohedral phases. The high frequency dielectric tensor is 6 and 5.1 for the cubic and rhombohedral phases, respectively.

3.3.2. Electron energy loss spectroscopy

For a wise interpretation, this plot and electron energy loss spectroscopy (EELS) should be brought together. Fig. 7 displays EELS spectra for the energy range of 0–35 eV. The function representing characteristic energy losses (or plasmon oscillations) is one of the most important among those suitable descriptions of microscopic and macroscopic properties of solids. This function is proportional to the probability that a fast electron moving in a medium loses energy, E, per unit length. For $LaCrO_3$, EELS is calculated from the dielectric function of just the x-polarization direction.

Generally speaking, the most prominent peak in the EELS spectrum is identified as the plasmon peak, signaling the energy of collective excitations of the electronic charge density in the crystal. It is possible to have several plasmon peaks in a crystal. In this context, we should also mention the occurrence of plasma resonances and their coupling to the spectra in Fig. 7. Plasma resonances manifest themselves as rather distinct peaks in the EELS, and are thus a feature that should be relatively easy to observe. However, they also have a simple relationship to the dispersive part of dielectric function [12]. A root in $\mathrm{Re}(\varepsilon)$, i.e. $\mathrm{Re}(\varepsilon)=0$, can give rise to a plasma resonance, although this is not a sufficient requirement. Damping of the plasma oscillations, so called Landau damping, may suppress the plasma peaks. Nevertheless, it is interesting to know the position of these roots.

In Fig. 6 we can identify four roots in the spectra for cubic phase, which are around 7, 12, 21 and 27 eV but, in Fig. 7, we identify two prominent peaks at energy 12 and 27 eV. These two peaks are related to the roots of dispersive spectra. These are plasma oscillation energies. However as is now obvious, not all roots to $\mathrm{Re}(\varepsilon)=0$ give rise to peaks in the electron energy loss spectrum. Thus, $\mathrm{Re}(\varepsilon)=0$ is a necessary condition for plasma oscillations to occur, but as observed is not a sufficient condition [12].

In Fig. 6 for rhombohedral phase, the roots are at energies of 7.8, 8, 12.6, 20.8 and 27 eV, whereas energies of 12.6 and 27 eV are due to plasma oscillations in the related EELS in Fig. 7.

The plasmon energy can be calculated according to the free electron theory:

$$\hbar\omega_p=\hbar\sqrt{ne^2/\varepsilon_0 m} \tag{11}$$

where n is the number of electronic per unit volume and m, the effective mass of the electron. Using the rest mass of electron, $m=m_0$ free electron theory works reasonably well for many systems. The effect of the underlying ion-core lattice on the plasmon energy can be included by using the effective mass, m^*, rather than m_0 [15]. Table 2 shows the comparison between plasmon energy calculated from free electron theory and the above plots in cubic and rhombohedral phases. Just, by considering valence electronic we reach to the value of 25 and by adding the contribution of La-5p semicore electron to the above formula, number of 27 is obtained. The same results between both structures are due to the same value of n which is equal to 0.47×10^{30} electrons/m^3 and 0.47×10^{30} for cubic and rhombohedral structures, respectively.

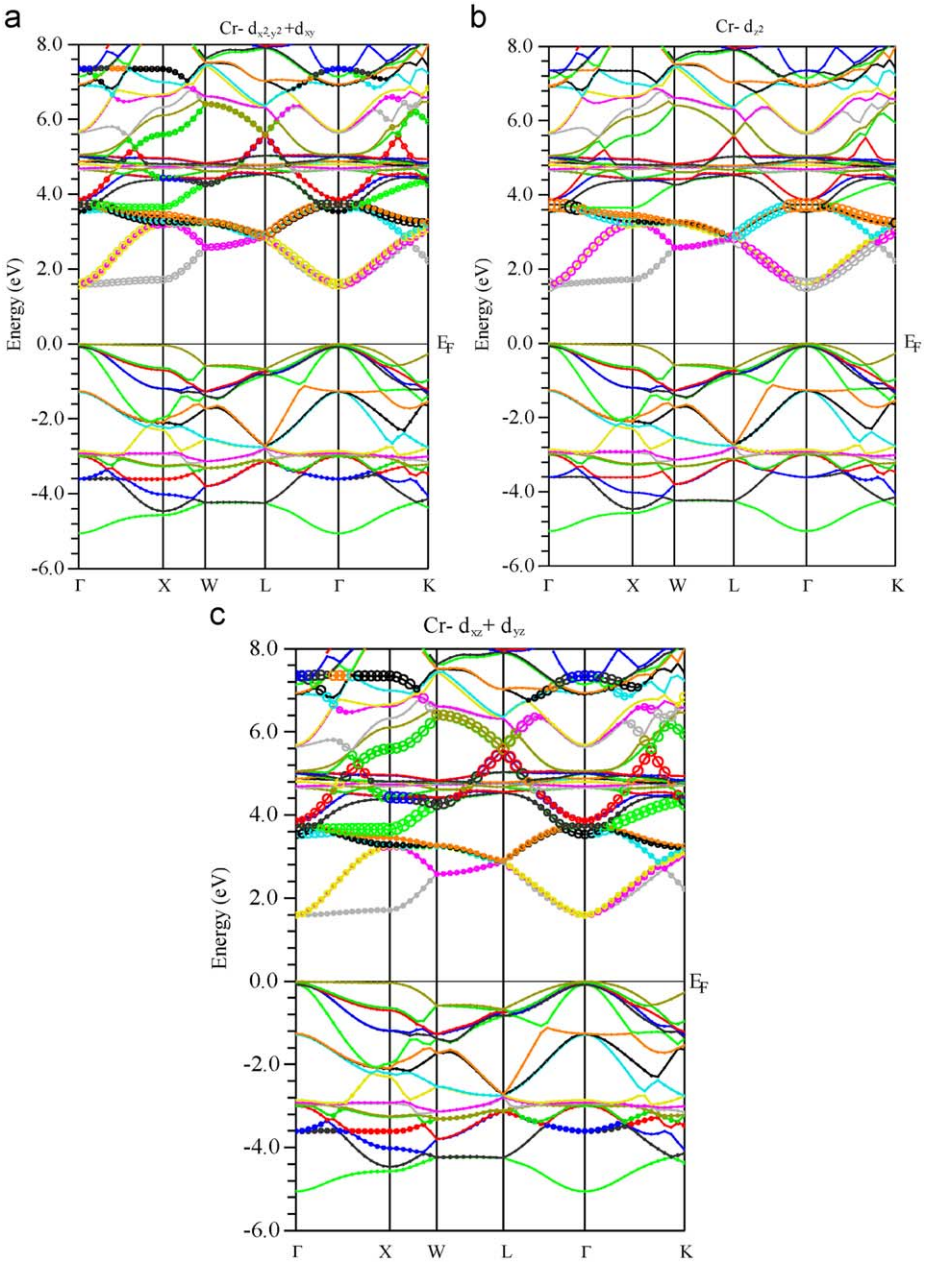

Fig. 4. Contribution of Cr-3d levels in band structure of $LaCrO_3$ in rhombohedral phase: (a) Cr-d_{x2-y2}+d_{xy} (b) Cr-d_{z2} (c) Cr-d_{xz}+d_{yz}.

3.3.3. Refractive index, extinction coefficient and optical reflectivity

The propagation of an electromagnetic wave through a material can be described by the complex refractive index $N(\omega) = n(\omega)+ik(\omega)$ which is mathematically related to $\varepsilon(\omega)$. n and k, which are the refractive index and the extinction coefficient, respectively, depend on the frequency of the incident radiation. In vacuum, N is real and equal to 1 and it is also real for transparent materials in the visible range, but it is complex for absorbing materials.

The reflectivity arises from the induced polarization current corresponding to the valence electrons oscillating out of phase with the incident radiation. There is no absorption for this process, but the interference of the incident beam with the waves reradiated by the valence electrons does lead to appreciable reflectivity [16].

Figs. 8 and 9 display the variation of n and k as a function of the incident radiation energy (E) for cubic and rhombohedral phases, respectively. The static refractive index is 2.25 and 2.27 for cubic and rhombohedral phases, respectively. The optical constants calculated in this work for $LaCrO_3$ are summarized in Table 3.

Fig. 10 displays reflectivity for cubic and rhombohedral phases. With the presence of extinction coefficient and reflectivity plots, we can define absorption, reflection and transparent regions. Peak of the extinction coefficient shows the region of absorption and peak of reflection displays the region of reflection. The regions where both plots of extinction and reflectivity are declined are called transparent. As we see for both structures, these properties are approximately the same. Table 4 shows approximately different regions of absorption, transparent and reflectivity for both structures.

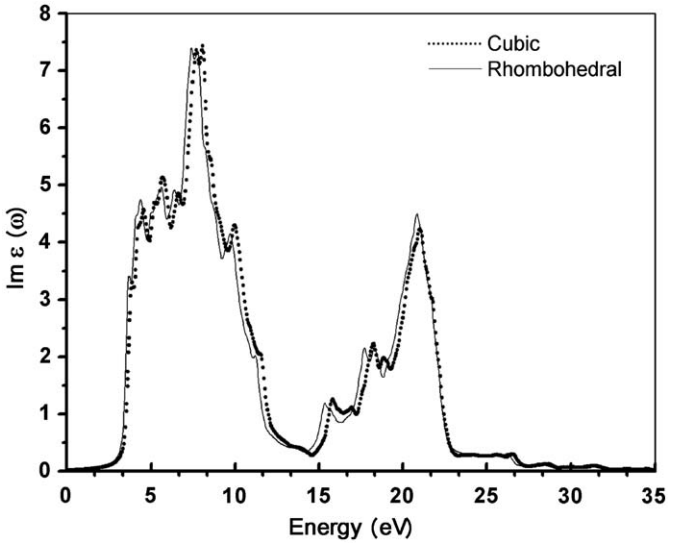

Fig. 5. Imaginary part of dielectric tensor in *x*-direction, for cubic and rhombohedral phases.

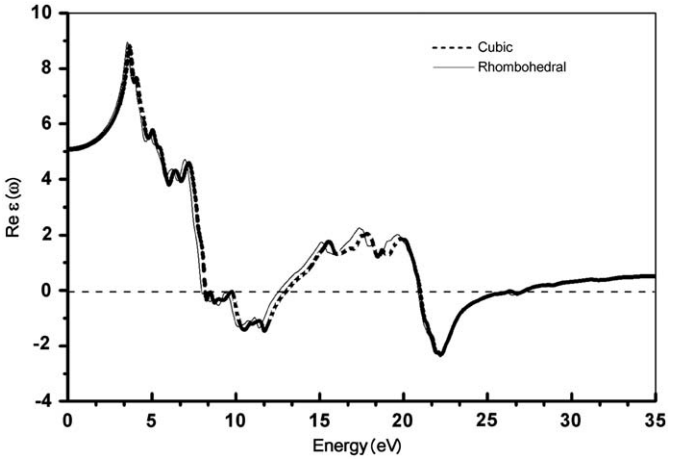

Fig. 6. Real part of dielectric tensor in *x*-direction, for cubic and rhombohedral phases.

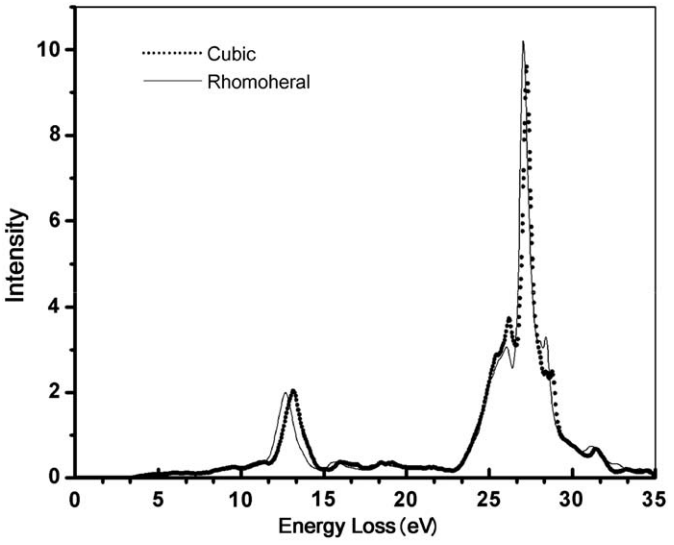

Fig. 7. Electron energy loss spectrum, for cubic and rhombohedral phases.

Table 2
Comparison between calculated plasmon energy according to free electron method and plasmon energy obtained by FP-LAPW approach.

Structure	Plasmon energy		
	FP-LAPW	Free electron (valence electrons)	Free electron (valence electrons+La-5p)
Cubic	27	25.5	27
Rhombohe-dral	27	25.0	27

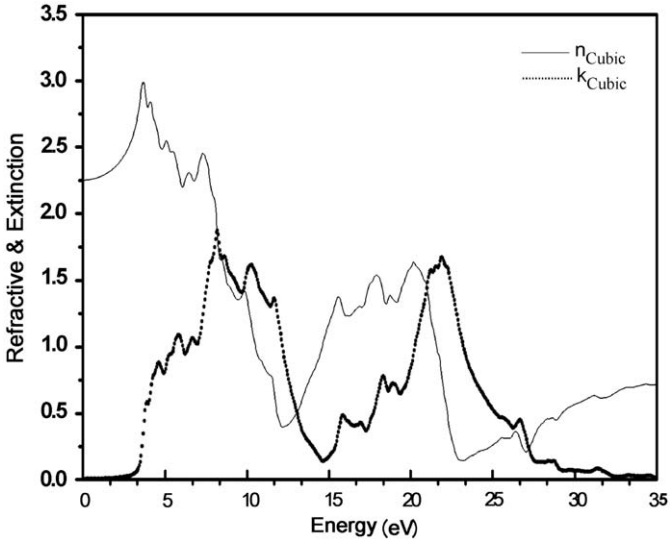

Fig. 8. Refractive index and extinction coefficient for $LaCrO_3$ in cubic phase.

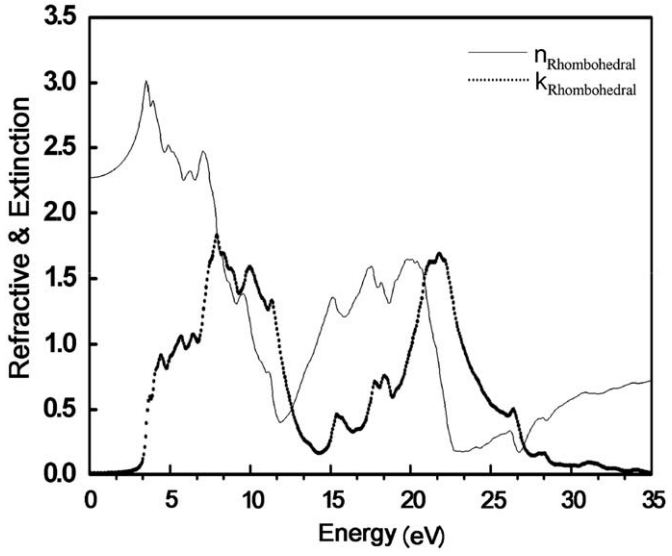

Fig. 9. Refractive index and extinction coefficient for $LaCrO_3$ in rhombohedral phase.

At last, it is apparent that the region lower than 3.17 and 3.06 eV (optical gap) is a transparent region for both structures.

3.3.4. Evaluating dispersion coefficients

Although the differences between cubic and rhombohedral plots are not obviously observed, we can show it better by plotting

Table 3
The refractive index and high-frequency dielectric constants for $LaCrO_3$ cubic and rhombohedral phases.

	$n(0)$		$\varepsilon(\infty)$	
Structure	Cubic	Rhombohedral	Cubic	Rhombohedral
This work	2.25	2.27	5.06	5.15

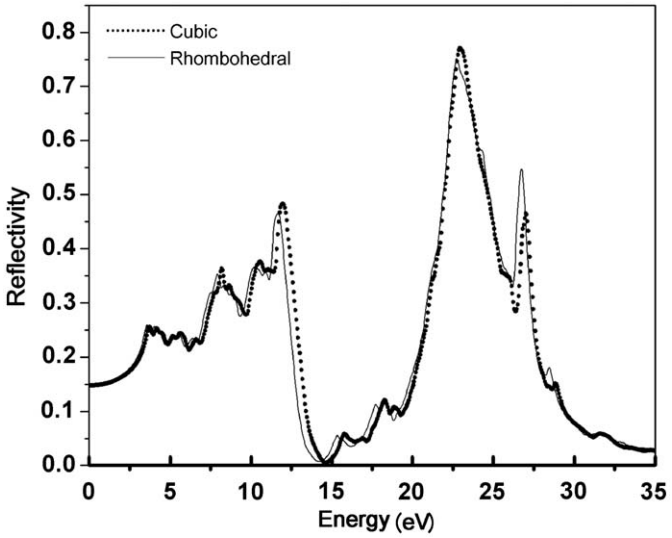

Fig. 10. Reflectivity of $LaCrO_3$ in cubic (dashed line) and rhombohedral phases.

Table 4
Approximated regions of transparent (T), absorption (A) and reflectivity (R) for both structures.

Regions	T	A	R	T	A, R	T	R	T
Energy (eV)	<3.5	3.5–6	6–13	13–15	15–22	22–27	27–28	28<

Table 5
The refractive indices of $LaCrO_3$ in cubic and rhombohedral phases.

Wavelength λ (μm)	n_{cubic}	$n_{rhombohedral}$
0.43	2.51	2.51
0.48	2.44	2.44
0.54	2.39	2.39
0.57	2.37	2.37
0.65	2.34	2.36

refractive index n versus wavelength λ (μm) and evaluating dispersion coefficients. Table 5 shows the refractive indices precisely at wavelength of 0.43, 0.54, 0.57, 0.48 and 0.65.

Figs. 11 and 12 show n values changing with wavelength for cubic and rhombohedral, respectively. Similar to other ABO_3 type perovskite structure compounds, $LaCrO_3$ crystal has large refractive indices and obvious dispersion relation, and its refractive indices decrease fast with the increasing wavelength.

The most important property of optical crystal is the refractive index and its dispersion behavior. Typical Sellmeier dispersion equation of crystal for refractive index is

$$n^2 = P_1 + \frac{P_2}{\lambda^2 + P_3} + P_4 \times \lambda^2 \quad (12)$$

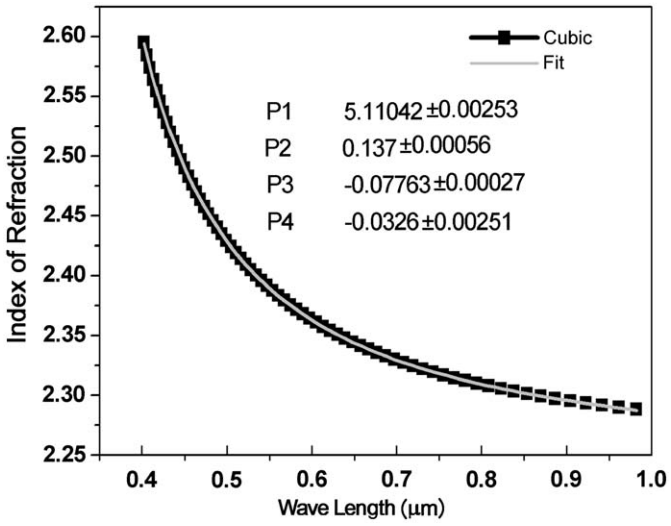

Fig. 11. Calculated refractive indices of $LaCrO_3$ in cubic phase at different wavelengths. Gray line is fitting of Sellmeier equation.

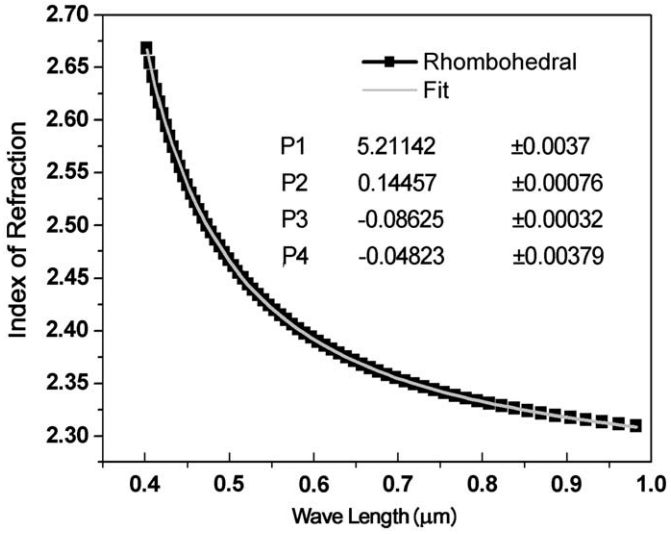

Fig. 12. Calculated refractive indices of $LaCrO_3$ in rhombohedral phase at different wavelengths. Gray line is fitting of Sellmeier equation.

where P_1, P_2, P_3 and P_4 are Sellmeier coefficients and constant. These coefficients are usually quoted for wavelength, λ, in micrometers. They can be obtained by the least squares fitting of Eq. (12). The gray line in Figs. 11 and 12 are the fitting results. Thus, Sellmeier dispersion equations for cubic and rhombohedral phases of $LaCrO_3$ are

$$n^2_{cubic} = 5.11042 + \frac{0.137}{\lambda^2 - 0.07763} - 0.0326 \times \lambda^2$$

$$n^2_{rhombohedral} = 5.21142 + \frac{0.14457}{\lambda^2 - 0.08625} - 0.0482 \times \lambda^2$$

Through these equations, we can get the refractive indices at other wavelengths. The dispersion curve is fairly flat in the long-wavelength region and rises rapidly at shorter wavelengths, showing the typical shape of dispersion curve near an electronic interband transition.

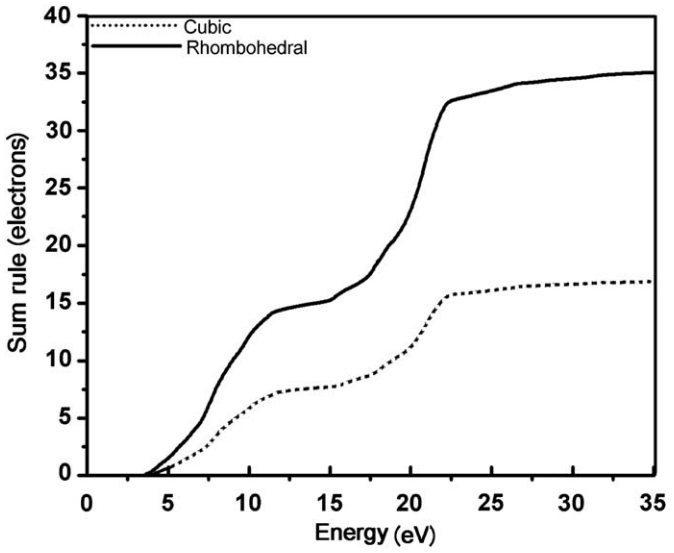

Fig. 13. Sum rules for $LaCrO_3$ in cubic and rhombohedral phases.

3.3.5. *Sum rule*

Fig. 13 displays sum rules for both phases of $LaCrO_3$, which give the effective number of electrons contributing to the absorption process as a function of energy. This number should never exceed the number of valence electrons for an energy that is below the first inner-shell ionization energy. For cubic and rhombohedral phases, respectively, numbers of electrons tend to the saturation value of 17 and 35 eV, up to energy of 40 eV. These values are lower than the number of valence electronic that are 27 and 54 in the conventional cells of cubic and rhombohedral phases, respectively.

In Fig. 13 there is a break in the curves before saturation and may be related to the onset of d-band excitations. Similar behavior has been observed in the 3–5 semiconductor compounds (i.e. GaAs, GaP and InSb) [17].

4. Conclusion

We present detailed nanoscale ab-initio calculations of the structural optical and electronic properties of perovskite $LaCrO_3$ in nonmagnetic cubic and rhombohedral phases, using the FP-LAPW method. The electronic structure, the imaginary and real parts of the dielectric function of $LaCrO_3$, electron energy loss spectroscopy, refraction index, extinction coefficient, reflectivity and sum rules have been discussed. We are not aware of any published experimental or theoretical data for these phases, so our calculation can be used to cover this lack of data for these phases. Also, our calculations show no clear discrepancy between optical and electronic properties of both structures, due to approximately the same ratio of valence electrons to the volume of primitive cell.

References

[1] R. Dogra, A.C. Junqueire, R.N. Saxena, A.W. Carbonari, J. Mestnik-Filho, M. Moralles, Phys. Rev. B 63 (2001) 224104.
[2] R. Ravindran, R. Vidya, H. Fjellvag, A. Kjekshus, J. Crystal Growth 268 (2004) 554.
[3] J.J. Neumeier, H. Terashita, Phys. Rev. B 70 (2004) 214435.
[4] K. Oikawa, T. Kamiyama, T. Hashimoto, Y. Shimojyo, Y. Morii, J. Solid State Chem. 154 (2000) 524.
[5] T. Armia, Y. Tokura, Phys. Rev. B 48 (1993) 17006.
[6] K.P. Ong, P. Blaha, P. Wu, Phys. Rev. B 77 (2008) 073102.
[7] S. Geller, P.M. Raccah, Phys. Rev. B 2 (1970) 1167.
[8] P. Blaha, K. Schwarz, G. Madsen, D. Kvasnicka, J. Luitz, Institute of Materials Chemistry TU Vienna, "WIEN2k", 〈www.wien2k.at〉.
[9] J.P. Perdew, K. Burke, Y. Wang, Phys. Rev. B 54 (1996) 16533.
[10] J.P. Perdew, S. Burke, M. Ernzerhof, Phys. Rev. Lett. 77 (1996) 3865.
[11] T. Kokalj, xcrysden program (x-window CRYstalline Structures and DENsities), 〈www.xcrysden.org〉.
[12] P. Ravindran, A. Delin, R. Ahuja, B. Johansson, S. Auluk, J.M. Wills, O. Eriksson, Phys. Rev. B 56 (1997) 6851.
[13] C. Ambrosch-Draxl, J.O. Sofo, J. Comput. Phys. 175 (2006) 1.
[14] F. Goubin, X. Rocquefelte, D. Pauwels, A. Tressaud, A. Demourgues, S. Jobic, Y. Motardi, J. Solid State Chem. 177 (2004) 2833.
[15] V.J. Keast, J. Electron Spectroscopy Related Phenomena 143 (2005) 97.
[16] F. Wooten, Optical Properties of Solids, vol. 51, Academic Press, INC, 1972 (Chapter 3).
[17] H.R. Philipp, H. Ehrenreich, Phys. Rev. 129 (1962) 1550.